Electronic Research Archive

ERA, 34(3): 1363–1385.
DOI: 10.3934/era.2026062
Received: 01 December 2025
Revised: 16 January 2026
Accepted: 28 January 2026
Published: 11 February 2026

https://www.aimspress.com/journal/ERA

Research article

A novel stochastic resonance based closed-loop neural network method for image segmentation

Di Wang[1], Yang Wang[2,*], Chunxia Lu[3], Zonglian Wang[4], Jiandun Chen[1] and Shanshan Xu[1]

[1] Westlake Institute for Optoelectronics, Hangzhou 311400, China
[2] College of Information Engineering, Taizhou University, Taizhou 225300, China
[3] Dingjie Shuzhi Co., Ltd., Nanjing 210012, China
[4] College of Mechanical and Electrical Engineering, China Jiliang University, Hangzhou 310018, China

* **Correspondence:** Email: wy23912@gmail.com; Tel: +8618030203344.

Abstract: Extracting multi-level information in colony images facilitates analysis and identification tasks of biomedical informatics. In order to achieve multi-level segmentation in colony images with multiple contrast levels, a closed-loop neural network model based on the stochastic resonance (SR) mechanism of neurons is proposed. First, this paper realizes the detection of transition pulses in sinusoidal, non-periodic bipolar binary signals, and one-dimensional strong and weak transition signals with multiple amplitude values. Then, through enhancement processing for the detection by the SR-based closed-loop neural network model, combined with the coati optimization algorithm, multi-target detection is achieved. Eventually, it can be applied to the segmentation of multi-level grayscale signals in two-dimensional images. Experimental results show that the proposed method can simultaneously detect strong and weak contrast edges, enrich image details, highlight image contours, and enhance the hierarchical sense of image edges, while exhibiting strong robustness against external noise. As a result, the proposed method provides a novel research framework for multi-contrast grayscale image segmentation under strong noise background.

Keywords: closed-loop neural network; stochastic resonance; coati optimization algorithm; image segmentation

1. Introduction

In the field of biomedical informatics, the effective extraction, analysis and identification of regions of interest in colony images are of great significance [1]. Since the colony images are characterized by multiple grayscale levels, it is necessary to extract multi-level information facilitating subsequent analysis and identification tasks [2,3]. Though the traditional image segmentation methods, achieving good results in low-noise environments, include methods based on differential threshold principles [4,5], directional wavelet transforms [6], morphology [7], and fuzzy theory [8], the edge information inevitably gets contaminated by noise due to lighting conditions and characteristics of the imaging subjects during image acquisition. When images contain strong noise, traditional segmentation methods tend to filter out useful image information while eliminating noise, resulting in unsatisfactory performance. In fact, the challenges for image segmentation, such as accurately extracting edges at different grayscale levels and distinguishing between different colony contents due to low contrast, are still not been completed. Therefore, it is necessary to develop an effective and precise method for multi-level grayscale segmentation of colony images to assist researchers in reducing the workload of colony segmentation tasks and accurately extracting target regions of interest.

In recent years, with the development of deep learning, some researchers have applied convolutional neural networks and various improved deep learning algorithms to achieve image segmentation results across different fields, demonstrating significant application potential. Ziang et al. [9] integrated an advanced UNet++ model based on U-Net, consisting of three main modules (i.e., data augmentation, optimized neural network, and parameters), achieving segmentation of lung regions in chest CT images. Arzvani et al. [10] proposed a hybrid method using FusionLungNet network for lung cancer diagnosis applications. This network features a multi-level structure containing key components, including ResNet-50 encoder, channel aggregation attention (CAA) module, multi-scale feature fusion (MFF) block, self-refinement module, and multiple decoders for fine-tuning. Zhu et al. [11] proposed a dual-branch ultrasound image segmentation network (DBUNet) based on the U-Net architecture in ultrasound applications, which consists of four main parts, i.e., enhancement branch, original branch, feature aggregation module, and decoder blocks. The enhancement branch combines signal processing techniques like filtering and histogram equalization with attention-based denoising. Chen et al. [12] proposed a supervised machine learning approach using convolutional neural networks to improve cell segmentation accuracy in the cell segmentation field. Du et al. [13] implemented an improved fusion rule and deep residual structure feature extraction network for precise segmentation of biological tissue images and non-target edge localization between multiple regions in medical images, achieving good experimental results with the improved segmentation algorithm and deep residual structure feature extraction network on medical images. The advantage of the above-mentioned methods is that the segmentation accuracy has been improved in many scenarios for target segmentation. However, the disadvantage is that some methods require large training samples and manual annotations, which is time-consuming and results in relatively low efficiency. Moreover, for the methods not relying on training, that achieving good segmentation results for multi-level images remains a challenging problem.

To address the above-mentioned problem, a closed-loop neural network model based on stochastic resonance (SR) mechanism is proposed. By utilizing the SR characteristic of neurons, a closed-loop series-parallel neural network is constructed to achieve multi-level grayscale image segmentation. The contributions are as follows:

1) We implement transition pulse detection for sinusoidal, non-periodic bipolar binary signals and one-dimensional strong/weak transition signals with multiple amplitude values.

2) Through the enhancement processing of transition pulse detection by the SR-based constructed closed-loop neural network model, multi-target detection is achieved by combining with the coati optimization algorithm (COA), and applied to the segmentation of multi-level grayscale signals in two-dimensional images, solving complex multi-level segmentation scenarios in biomedical images.

3) Experimental results show that the proposed method can simultaneously detect strong and weak contrast edges, enrich image details, highlight image contours, enhance the hierarchical sense of image edges, and exhibits strong robustness against external noise. Compared with other methods, the proposed method shows significant improvement in term of multiple contrast edge image segmentation of images under strong noise background without large training samples.

2. Stochastic resonance mechanism based closed-loop neural network model

2.1. Fitzhugh-Nagum neuron model

The Fitzhugh-Nagum (FHN) neuron model is a nonlinear excitable cell model, which is a simplified model of Hodgkin-Huxley (H-H) neurons, and has the characteristics of neurophysiological SR [14–17]. Its differential expression satisfies the zero initial condition and can be described by

$$\begin{cases} \varepsilon \dfrac{v(t)-v(t-\Delta t)}{\Delta t}=v(t)(v(t)-a)(1-v(t))-w(t)+A_T-B+I_{ext}(t) \\ \dfrac{w(t)-w(t-\Delta t)}{\Delta t}=\gamma(v(t)-w(t)-b) \end{cases} \tag{2.1}$$

where $v(t)$ is the fast-changing membrane potential of the neuron at time t, $w(t)$ is the slow-changing recovery variable at time t, the time constants ε and γ determine the firing rate of the neuron, A_T is the threshold value that prompts the neuron to fire periodically, B is the difference between the average signal level and A_T, a and b are the constants, and $I_{ext}(t)$ is the external current input at time t.

2.2. Closed-loop Fitzhugh-Nagum neural network model

In fact, different network models for image denoising have been developed by the usage of FHN neurons [18]. Although the open-loop series FHN neural network model (shown in Figure 1) can better describe the characteristics of synaptic multi-input connections and continuous transmission of action potentials, its essence is a SR mechanism that cannot meet the segmentation of multi-contrast images.

To address this problem, in Figure 2, we propose a closed-loop FHN neural network model based on SR mechanism, which can be expressed as

$$\begin{cases} \varepsilon_1 \dfrac{v_{1,i}(t)-v_{1,i}(t-\Delta t)}{\Delta t}=v_{1,i}(t)(v_{1,i}(t)-a_1)(1-v_{1,i}(t))-w_{1,i}(t)+A_{T1}-B_1+I_{ext}(t) \\ \dfrac{w_{1,i}(t)-w_{1,i}(t-\Delta t)}{\Delta t}=\gamma_1(v_{1,i}(t)-w_{1,i}(t)-b_1) \end{cases}$$

$$\begin{cases} \varepsilon_2 \dfrac{v_{2,j}(t)-v_{2,j}(t-\Delta t)}{\Delta t}=v_{2,j}(t)(v_{2,j}(t)-a_2)(1-v_{2,j}(t))-w_{2,j}(t)+A_{T2}-B_2+v_{2,j-1}(t) \\ \dfrac{w_{2,j}(t)-w_{2,j}(t-\Delta t)}{\Delta t}=\gamma_2(v_{2,j}(t)-w_{2,j}(t)-b_2) \end{cases}, \tag{2.2}$$

where $v_{1,i}(t)\,(i=1,2,\cdots,k_1)$ and $v_{2,j}(t)\,(j=1,2,\cdots,k_2)$ represent the fast-changing membrane potentials of the parallel module and the series module at time t, respectively. k_1 denotes the number of FHN neurons in the parallel module, while k_2 denotes the number of FHN neurons in the series module. $w_{1,i}(t)(i=1,2,\cdots,k_1)$ and $w_{2,j}(t)(j=1,2,\cdots,k_2)$ represent the slow-changing recovery variables of the parallel module and the series module at time t, respectively. ε_m and γ_m are time constants that determine the firing rate of the neurons. A_{Tm} is the threshold value that prompts the neurons to fire periodically. B_m is the difference between the average signal level and A_{Tm}. a_m and b_m are constants with $m=1,2$. $I_{ext}(t)$ is the external current input at time t. As a matter of fact, when $j=1$, $v_{2,j-1}(t)=v_{2,0}(t)=1/k_1\sum_{i=1}^{i=k_1}v_{1,i}(t)$, meaning that the average output of the k_1 FHN neurons in the parallel module serves as the input to the first FHN neuron in the series module. When $2\le j\le k_2$, $v_{2,j-1}(t)$ represents the output value of the $j-1$ neuron in the series module.

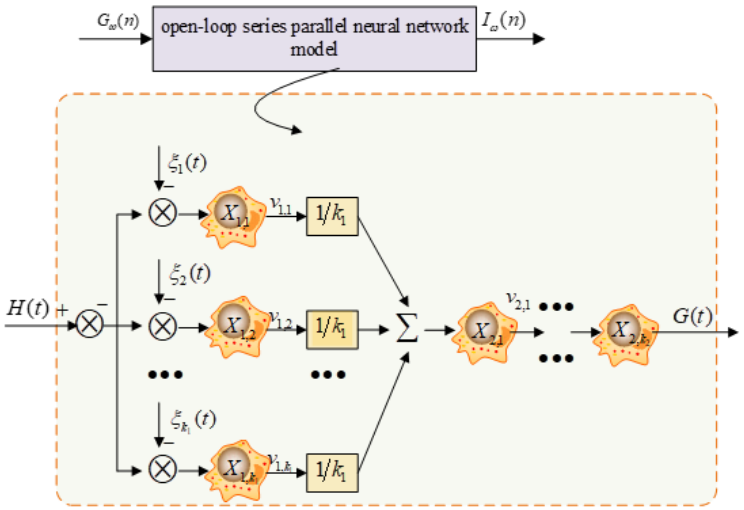

Figure 1. Open-loop series parallel FHN neural network model.

As seen in Figure 2, $X_{1,i}$ and $X_{2,j}$ represent the FHN neuron models of the parallel module and the series module, respectively. $\xi_i(t)$ denotes the internal Gaussian white noise of $X_{1,i}$, satisfying the conditions $\langle\xi(t)\rangle=0$ and $\langle\xi(t_1)\xi(t_2)\rangle=2D_i\delta(t_1-t_2)$, where D_i is the noise intensity. $H(t)$ represents the one-dimensional input signal sequence of the closed-loop FHN neural network model. During the first SR modulation, the external current input is $I_{ext}(t)=H(t)+\xi_i(t)$. After processing by

$X_{1,i}$ and $X_{2,j}$, the one-dimensional output sequence $G(t)$ is obtained. During the second SR modulation, the external current input is $I_{ext}(t) = H(t) + \xi_i(t) + \lambda G(t)$ (where λ is the feedback coefficient). After processing again by $X_{1,i}$ and $X_{2,j}$, a new one-dimensional output sequence $G(t)$ is obtained. At this stage, $G(t)$ represents the final output sequence of $H(t)$ processed by the closed-loop FHN neural network model.

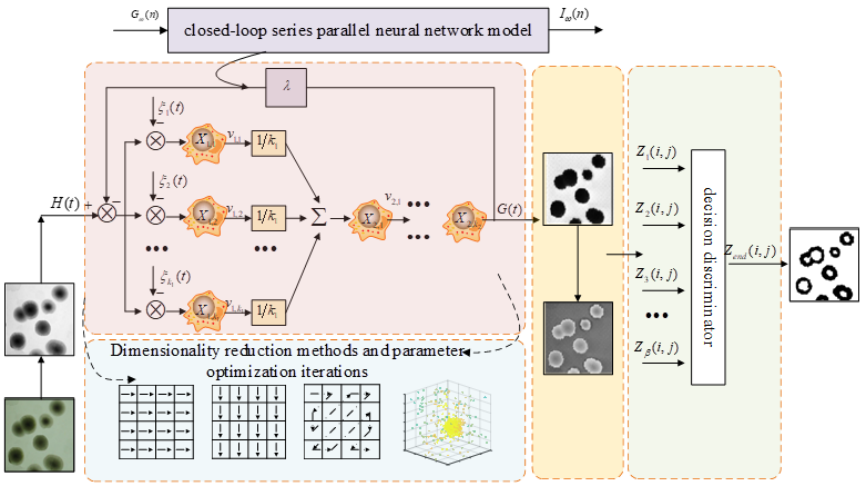

Figure 2. Closed-loop series parallel FHN neural network model.

2.3. Coati optimization algorithm for stochastic resonance based neural network model

Since the parameter selection of the SR mechanism plays a crucial role in signal enhancement, Coati optimization algorithm (COA) [19] is adopted for identifying optimal parameters for the proposed model to perform image segmentation. COA is primarily employed to optimize parameters *a* and *b* of the FHN neuron model and the internal noise, which are inherent properties of the system. By leveraging the balanced capability of COA for global exploration and local optimization, adaptive optimization of multiple parameters in the SR system is achieved. Compared to traditional ant colony optimization algorithms, COA demonstrates more pronounced resonance effects in SR systems.

Specifically, COA is used to optimize parameters *a* and *b* in the adaptive SR system, with settings such as population size *N*, maximum iteration count *T*, and fitness value for each individual [19]. For segmentation, multi-level segmentation primarily focuses on pulse detection of transition signals. A higher number of detected transition pulses indicates richer edge detection. Therefore, the number of transition pulses is adopted as the evaluation function in the optimization process of COA. The workflow of the adaptive SR system based on COA is illustrated in Figure 3.

In COA, the coati adaptive parameter optimization process consists of two phases. The first phase is the coati's hunting and attacking stage (i.e., global search), where the first half of the population climbs trees to drive prey, and the second half of them wait on the ground to attack the prey once it falls. The positions (*a*,*b*) of the coatis are continuously updated. If a new position improves the value of the objective function, the new position is accepted; otherwise, the coati retains its previous position (i.e., a greedy selection is performed). The second phase is the coati escaping from the predator's stage (i.e., local search). When a predator attacks the coati, it flees from its current position. The change in

the coati's position triggers a greedy selection. Through continuous iterations of local optimization, the global optimal parameters are ultimately obtained.

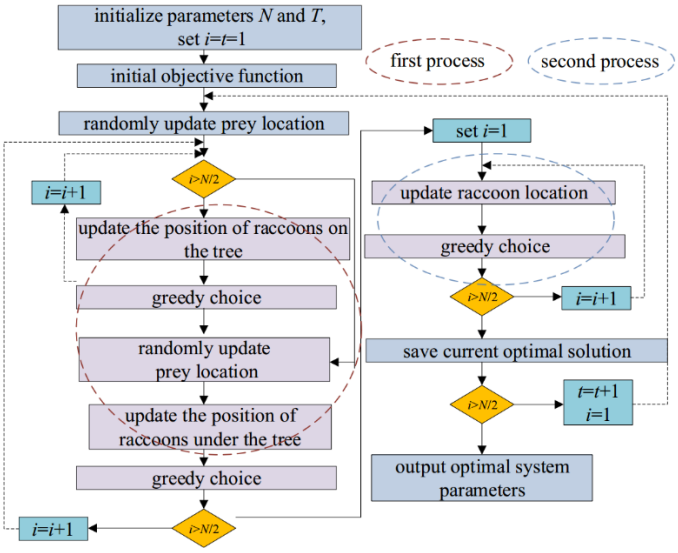

Figure 3. COA for SR based neural network model.

2.4. Detection of strong and weak jumps in one-dimensional periodic signals

First, a closed-loop FHN neural network model is employed to detect strong and weak transitions in one-dimensional sine signals. The input signals are $I_{\text{strong}} = A_1 \sin(2\pi f_s t) + \xi(t)$ and $I_{\text{weak}} = A_2 \sin(2\pi f_s t) + \xi(t)$, where $A_1 = 0.4$, $A_2 = 0.1$, and the internal noise intensity $D_{in} = 0.5$. Here, $\xi(t)$ represents externally added Gaussian white noise, satisfying the aforementioned noise conditions, with the external noise intensity of $D_{\text{out}} = 0.4$. The frequency is set to $f_s = 50Hz$. The system parameters are configured as follows: the pulse threshold is $thre = 1.4$, the feedback coefficient is $\lambda = 0.2$, $\varepsilon = 1$, $\gamma = 0.01$, $a = 0.1$, $b = 0$, and $AT - B = 0\text{mv}$. The fast-changing membrane potential and slow recovery variable of the neuron satisfy the zero initial value condition. For intuitive display, an open-loop FHN neural network model based on the SR mechanism is compared with the proposed model, which is shown in Figure 4.

As seen in Figure 4(c), there are pulse outputs at the peaks of the sine signal with an amplitude of 0.4 in the open-loop model based on the single SR mechanism, indicating that strong jump signals can be detected. However, the sine signal with an amplitude of 0.1 only has corresponding pulse outputs at two peaks, indicating poor detection performance for weak jump signals. From Figure 4(d), it can be seen that both strong and weak jump signals can be detected by the closed-loop model based on the dual SR mechanism. Based on the above experimental results, it can be concluded that for one-dimensional sine signals, the open-loop model based on the SR mechanism can only detect strong jump signals, that is, can only detect strong contrast edges. The closed-loop model based on the SR mechanism performs well in detecting strong and weak transition signals, that is, it can simultaneously detect strong and weak contrast edges.

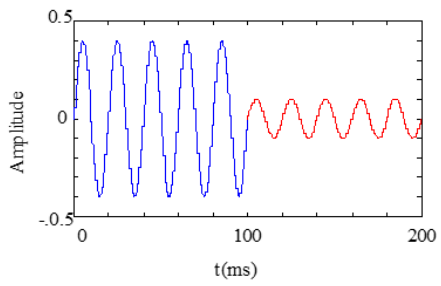

(a) Original periodic sine signal.

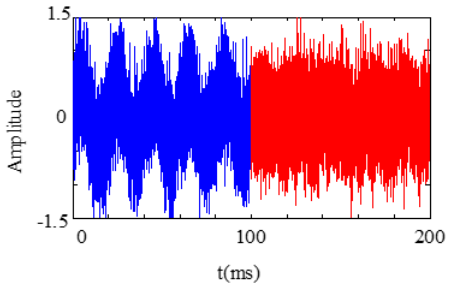

(b) The signal with external noise intensity 0.4.

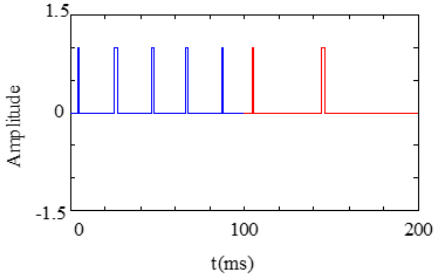

(c) Detection results by open-loop model for (b).

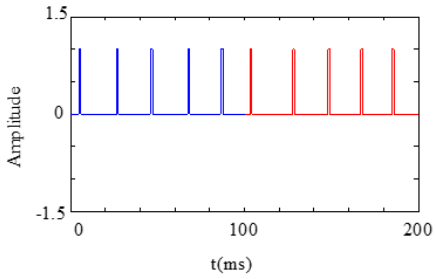

(d) Detection results by closed-loop model for (b).

Figure 4. Detection results by different neural network model.

2.5. Strength jump detection for one dimensional non-periodic bipolar signal

For one-dimensional aperiodic signals, a binary bipolar signal $S(t)$ is used as the noise-free aperiodic input signal of the system, where

$$S(t) = A \cdot \sum_{j=-\infty}^{\infty} S_j \Gamma(t - jT_j), \tag{2.3}$$

where the signal amplitude $A > 0$ is a constant, and $\Gamma(t) = \begin{cases} 1, & t \in [0, T_j] \\ 0, & other \end{cases}$ with the pulse width of signal $T_j = 500$, and $S_j = \pm 1$ is an independently distributed random variable. The system parameters are set consistently with those in Section 1.3 for strong and weak transition detection of periodic signals. The input signal amplitudes are $A_{\text{strong}} = 0.4$ and $A_{\text{weak}} = 0.2$, respectively, with an internal noise intensity of $D = 0.5$. Gaussian white noise with an external noise intensity of $D_{out} = 0.2$ is applied to the aperiodic signal. The experimental results are shown in Figure 5.

Comparing Figure 5 (c),(d), similar conclusions can be drawn to that in Section 2.4. The open-loop model can detect strong transitions for one-dimensional non-periodic signals, but with poor detection performance for weak transitions. That is, it can only detect strong contrast edges. The closed-loop model performs well in detecting both strong and weak transition signals, that is, it can simultaneously detect strong and weak contrast edges.

In fact, the area with severe grayscale changes (i.e., strong jump signals) is the strong contrast edge, and the area with gentle grayscale changes (i.e., weak jump signals) is the weak contrast edge. Based on the detection results of strong and weak jump signals in one-dimensional periodic signals and one-dimensional non-periodic signals, extending to two-dimensional image signals, it can be

inferred that the closed-loop FHN neural network model based on the dual SR mechanism theoretically has the possibility of detecting strong and weak contrast edges.

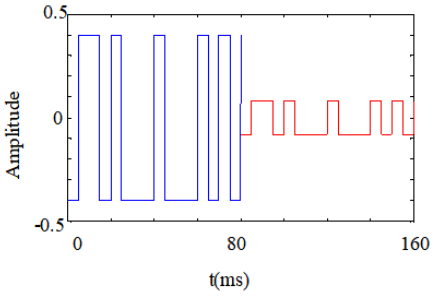

(a) Original non periodic signal.

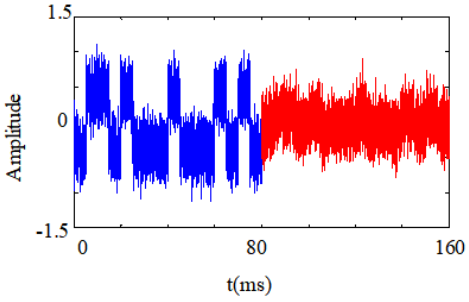

(b) External noise is 0.2, including noisy signals.

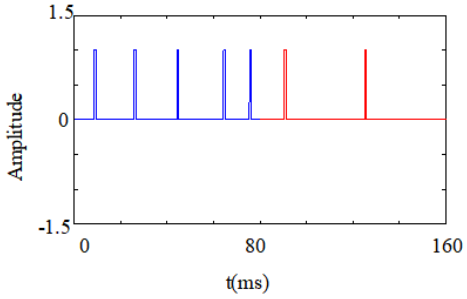

(c) Detection results for open-loop model for (b).

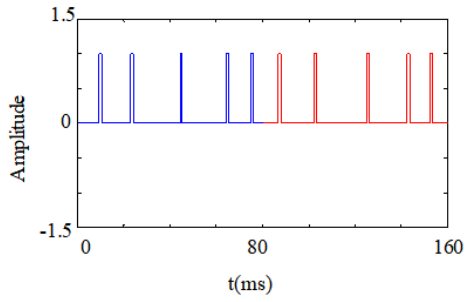

(d) Detection results by closed-loop model for (b).

Figure 5. Detection results by using different FHN neural network models.

2.6. Jump detection for one-dimensional multi-amplitude signal

Gray values of 0.4 and 0.3 are used to represent different contrast levels of the target objects in the image, while 0 represents the gray value of the background area. The weak edge between the target and the background is represented by the transition signal from 0.4 to 0, and the weak edge between different contrast regions within the same target is represented by the transition signal from 0.4 to 0.3. A one-dimensional multi-amplitude weak transition signal is constructed by

$$x(t)=\begin{cases}0, & nT\le t<nT+\dfrac{T}{2}\\ 0.4, & nT+\dfrac{T}{2}\le t<nT+\dfrac{3T}{4}\\ 0.3, & nT+\dfrac{3T}{4}\le t<nT+T\end{cases}\qquad n=0,1,2\cdots k_1, \tag{2.4}$$

where $T=40\text{ms}$ is the period of the square wave and $k_1=6$ means the original input signal in this experiment consisting of 7 cycles. To meet the bipolar requirement of the FHN neuron, let $x(t)=x(t)-0.2$, as shown in Figure 5(a). The internal noise intensity for SR is D=0.5, and $\xi(t)$ represents externally-added Gaussian white noise, satisfying the aforementioned noise conditions, with an external noise intensity of $D_{out}=0.2$. The system parameters are set as follows: pulse threshold

$thre = 1.5$ (a pulse is emitted if a strong transition signal with an amplitude of 1.5 is detected), $\varepsilon = 1$, $\gamma = 0.01$, $a = 0.1$, $b = 0$, and $AT - B = 0$mv. The fast-changing membrane potential and slow recovery variable of the neuron satisfy the zero initial value condition.

A multi-layer FHN neural network model based on a multi-level SR mechanism (with γ=2) is selected for the experiment, and the results are shown in Figure 6. As seen, Figure 6(a) shows the original signal with multi-level amplitude characteristics, Figure 6(b) shows the mixed signal of Gaussian white noise with an intensity of 0.2 added to Figure 6(a), and Figure 6(c) shows the processing result of the open-loop FHN series parallel neural network. It can be seen that the processing of the series-parallel FHN SR based neural network model can remove the noise signal and enhance the characteristics of the signal. Figure 6(d) shows the result of pulse detection for jump detection in Figure 6(c), and it can be seen that some signals with peak and valley abrupt changes are not completely detected. Figure 6(e) shows the subtraction result between Figure 6(a),(c). Figure 6(f) performs strong jump detection on Figure 6(e), and it can be seen that the richness of detection is greater than that of Figure 6(c), indicating that the detection of jump signals enhanced by the SR-based neural networks is more accurate.

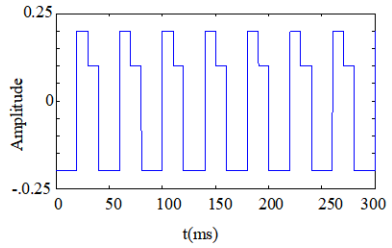

(a) original signal.

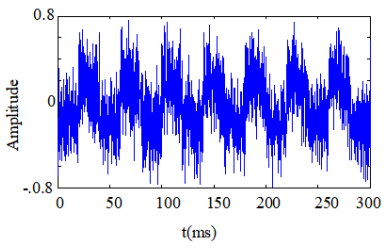

(b) Mixed signal with noise.

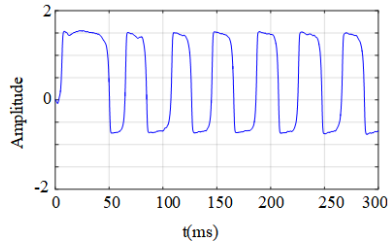

(c) Open loop FHN series parallel neural network processing.

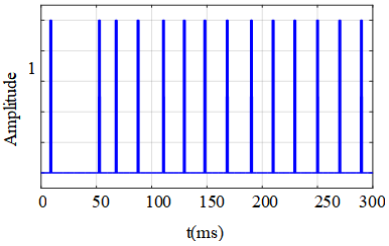

(d)For (c) jump detection pulse.

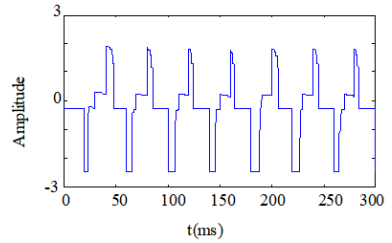

(e) (a) Subtraction result from (c).

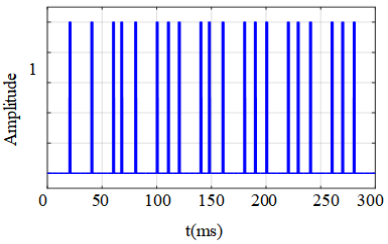

(f) Strong jump detection results for (e).

Figure 6. Detection results of one-dimensional square wave signal jump by closed-loop FHN neural network model.

3. Jump detection of multi-amplitude signals by closed-loop neural network model

The steps of the multi-amplitude jump detection algorithm based on the adaptive closed-loop

neural network model are as follows:

1) Read the original image and perform grayscale conversion to obtain $B(i,j)$, where $i=1,2,\cdots M$ (M represents the number of image rows) and $j=1,2,\cdots N$ (N represents the number of image columns). The following i and j are the same.).

2) To meet the bipolar requirements of the FHN neuron, apply linear stretching to $F(i,j)$ according to Eq (2.3), mapping the grayscale levels to the range [–128, 127], denoted as

$$P(i,j)=\frac{B(i,j)-\min(B(i,j))}{\max(B(i,j))-\min(B(i,j))}\times 255-128, \tag{2.5}$$

where $\max(B(i,j))$ and $\min(B(i,j))$ represent the maximum and minimum of $B(i,j)$, respectively.

3) Rotate $P(i,j)$ counterclockwise by 0°, 45°, 90°, and 135° to obtain four sets of two-dimensional signals $F_{\omega}(i,j)$ (where ω = 0°, 45°, 90°, 135°; the same applies to ω below). Then, perform Hilbert dimensionality reduction on $F_{\omega}(i,j)$ to obtain four sets of one-dimensional signal sequences, $h_{\omega}(n)$ (where $n=1,2\cdots M\times N$; the same applies below).

4) Pass $h_{\omega}(n)$ through the constructed FHN neural network model to obtain four sets of one-dimensional output sequences $e_{\omega}(n)$. Perform Hilbert reconstruction and clockwise rotation by the corresponding angles on $e_{\omega}(n)$ to obtain $Q_{\omega}(i,j)$.

5) Calculate the average value of $Q_{\omega}(i,j)$, denoted as $R(i,j)$. Perform raster scanning at angles of 0° and 90° on $R(i,j)$ to obtain two one-dimensional signal sequences, denoted as $l_{row}(n)$ and $l_{col}(n)$. Pass $l_{row}(n)$ and $l_{col}(n)$ through the FHN neurons to obtain two one-dimensional output signal sequences: $g_{row}(n)$ an $g_{col}(n)$. Reconstruct these into two-dimensional signals through raster scanning at 0° and 90°, denoted as $E_{row}(i,j)$ and $E_{col}(i,j)$, respectively.

6) Pass $E_{row}(i,j)$ and $E_{col}(i,j)$ through a discriminator O for decision fusion, obtaining a single two-dimensional signal denoted as $Z(i,j)$. The decision rule of O is given by

$$Z(i,j)=\begin{cases}E_{row}(i,j), E_{row}(i,j)>=E_{col}(i,j)\\ E_{col}(i,j), E_{row}(i,j)<E_{col}(i,j)\end{cases}. \tag{2.6}$$

7) Subtract $Z(i,j)$ from $P(i,j)$ (where λ is calculated as the ratio of 127, the maximum of $P(i,j)$, to the maximum value $\max_{z(i,j)}$ of $Z(i,j)$ to form a new input, i.e., $P(i,j)=P(i,j)-\lambda Z(i,j)$. Repeat steps (3) to (6) to obtain $Z(i,j)$ again, denoted as $U(i,j)$.

8) Use the obtained number of edge pulses as the optimal fitness function. Initialize the best fitness function and calculate the fitness function value $fitness(X)$ for each hybrid position. Non-global best fitness values are replaced by the best $fitness(X)$ of each generation and recorded as $pbest(i)(i=1,2,...,M)$. Set the global optimal fitness function, denoted as pbest, to be replaced by the maximum value among the local optima $pbest(i)$ of each hybrid position.

9) After completing step 8), the COA algorithm is applied to iteratively optimize the processing results multiple times, ultimately obtaining the maximum number of pulse responses and the processed image $U_{best}(i,j)$.

10) Perform thresholding on $U_{best}(i,j)$. The binarization rule is shown in Eq (2.7), which represents the final image segmentation result, expressed as

$$O(i,j)=\begin{cases}1, U_{best}(i,j)>=0\\ 0, U_{best}(i,j)<0\end{cases}. \tag{2.7}$$

4. Experimental results and analysis

The colony images shown in Figure 7 are used as the research objects. As seen in Figure 7, these colony images all have multi-level grayscale edges, which is also the multi-level segmentation problem that needs to be solved. The colony images were collected by our laboratory based on the needs of conventional microbiology experiments. A simulated natural light suspended dark field system was used, and an F/1.4 large aperture lens was used to image the colonies grown on the Petri dish after cultivation at the tens of millions of pixels level.

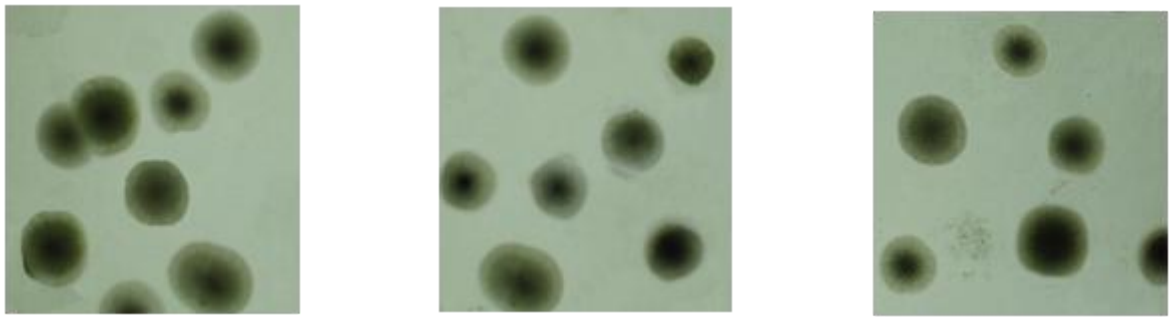

(a) (b) (c)

Figure 7. Original colony images.

Taking Figure 7(a) as an example, this proposed method first grayscales the original image to obtain Figure 8(a). By utilizing the SR mechanism to segment Figure 8(a), the colony image features used in this experiment are characterized by low grayscale values in the colony target area and high grayscale values in the background area. SR modulation was applied to Figure 8(a), causing the areas with low grayscale values (colony areas) to become lower, and the areas with high grayscale values (background areas) to become higher. Therefore, effective segmentation of colony targets and background areas can be achieved, as shown in Figure 8(b); Subtracting Figure 8(a) from Figure 8(b) yields Figure 8(c). The feature of Figure 8(c) is that the grayscale values of the background area and the strong contrast area of the colony target are very low, while the grayscale values of the weak contrast area of the colony target in Figure 8(c) are relatively high. By utilizing the SR mechanism again to modulate Figure 8(c), Figure 8(d) is obtained. The areas with low grayscale values are lower, while the areas with high grayscale values are higher, effectively achieving the segmentation of background areas, colony strong contrast areas, and colony weak contrast areas. Finally, thresholding was applied to Figure 8(c) to obtain Figure 8(d), resulting in better contrast and visual effects in colony segmentation.

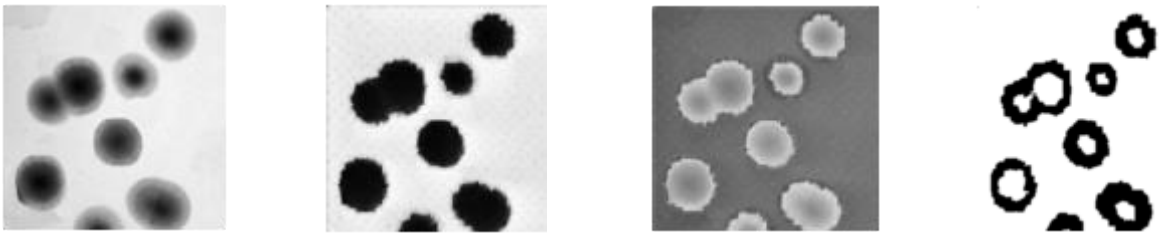

(a) Grayscale the original image. (b) Stochastic resonance modulation on (a). (c) Subtract (b) from (a). (d) Threshold processing for (c).

Figure 8. Schematic diagram of principle of the proposed method.

We conducted edge jump pulse detection on Figure 7(a) using the proposed four-channel *Hilbert* dimensionality reduction one-dimensional signal. We used coati optimization parameters a and b, as well as internal noise intensity D. As shown in Figure 9, the parameter optimization curves of the COA algorithm with internal noise intensity D=0.5, 1, 1.5, 2 are given. As seen, the series-parallel FHN neural network model has the characteristic of SR, and increasing the internal noise intensity can assist in the conversion of noise energy, enhancing the peak signal-to-noise ratio of useful signals, and transforming external noise to highlight useful signals.

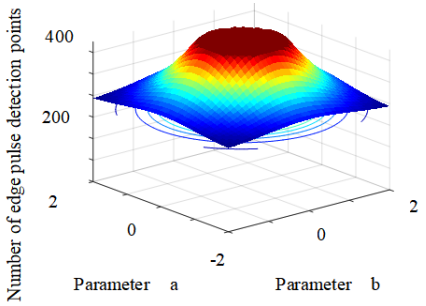

(a) Parameter optimization curve with D = 0.5.

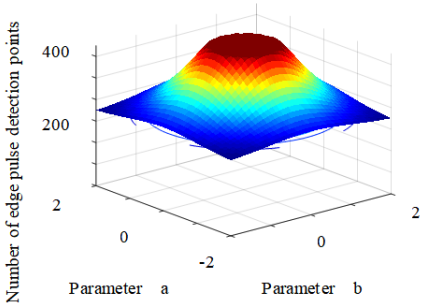

(b) Parameter optimization curve with D = 1.

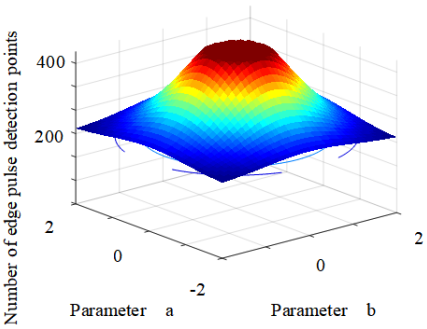

(c) Parameter optimization curve with D = 1.5.

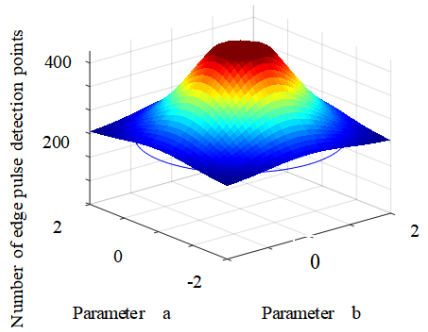

(d) Parameter optimization curve with D = 2.

Figure 9. Parameter optimization curves for selected four values of internal noises.

The noise intensity within the system is selected as 1.5 for the experiment, and two cutting-edge research methods in the relevant biomedical field, i.e., the adaptive contextual information-based 2D-

histogram algorithm (ACIH) [20], the hybrid bee-pollinator algorithm (HBPA) [21], and the UNet++ method proposed in [9] are chosen for comparison. From Figures 10–12, it can be observed that the ACIH segmentation method has a small amount of residual noise when segmenting colony targets. For example, when segmenting Figure 7(c), the stain in the lower left corner of the original image was not filtered out. The HBPA method, UNet++ method, and open-loop FHN network model maintain good geometric shape and smooth edges for colony segmentation, and weak noise is basically filtered out. However, they cannot achieve effective segmentation of colony targets in areas with strong and weak contrast.

(a) ACIH. (b) HBPA. (c) UNet++. (d) Open-loop FHN network model. (e) ours.

Figure 10. Segmentation effects on Figure 7(a) by different methods.

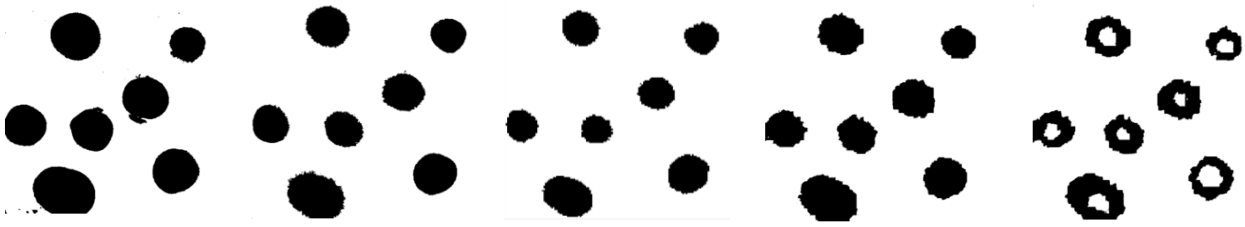

(a) ACIH. (b) HBPA. (c) UNet++. (d) Open-loop FHN network model. (e) ours.

Figure 11. Segmentation effects on Figure 7(b) by different methods.

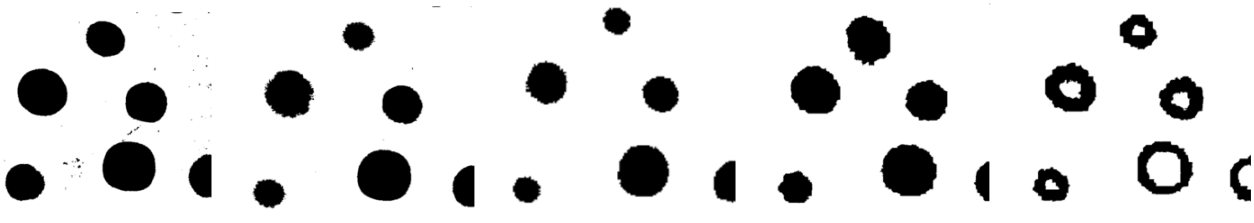

(a) ACIH. (b) HBPA. (c) UNet++. (d) Open-loop FHN network model. (e) ours.

Figure 12. Segmentation effects on Figure 7(c) by different methods.

Differently, the proposed method adopts a closed-loop FHN network model, which essentially creates a SR mechanism model. In fact, the internal and external noises are key parameters. First, the

internal noise is studied; the internal noise intensity (denoted as D) of the two SR systems is set to 1, 2, and 3, respectively. Experiments are conducted on the three colony object images in Figure 7, and the segmentation results are shown in Figures 13–15. Comparing the horizontal effect images in Figures 13–15, we can obtain that when the internal noise D is enhanced from 1 to 3, the image segmentation effect is almost unaffected, but, overall, the image segmentation effect is still good. The above experimental results qualitatively demonstrate that the SR mechanism used in this method has good robustness to internal noise.

(a) $D = 1$. (b) $D = 2$. (c) $D = 3$.

Figure 13. Segmentation effects on Figure 7(a) by the proposed method with $D = 1, 2, 3$.

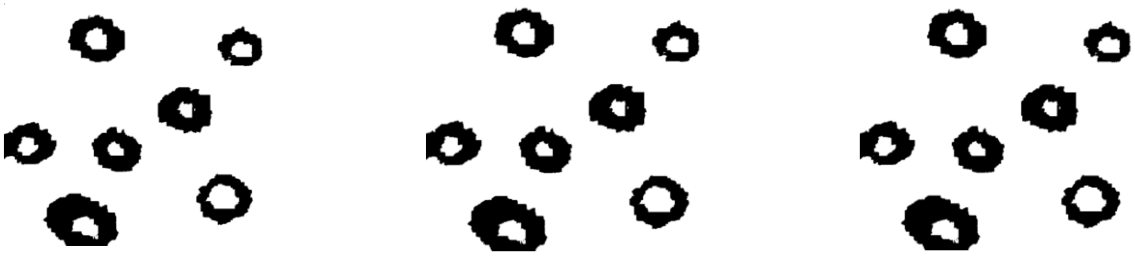

(a) $D = 1$. (b) $D = 2$. (c) $D = 3$.

Figure 14. Segmentation effects on Figure 7(b) by the proposed method with $D = 1, 2, 3$.

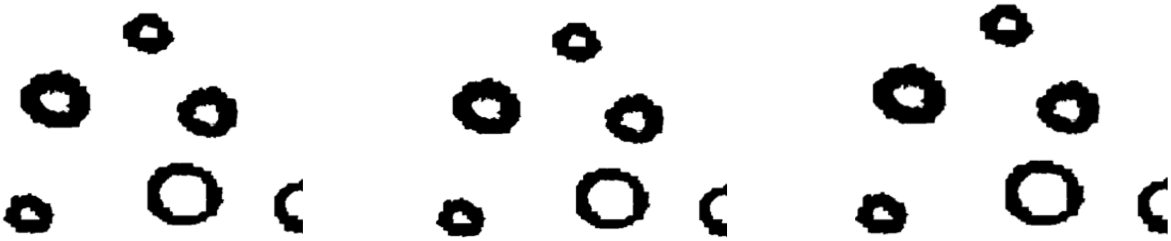

(a) $D = 1$. (b) $D = 2$. (c) $D = 3$.

Figure 15. Segmentation effects on Figure 7(c) by the proposed method with $D = 1, 2, 3$.

In order to better analyze the impact of internal noise on the SR the mechanism, the peak signal-to-noise ratio (PSNR) [22, 23] and the number of edge jump pulses (denoted as COUNT) as quantitative indicators are used. The intensity of internal noise D ranges from 0 to 5 to measure the effectiveness of SR. The results are shown in Table 1. To further present the visual effect, the two

indicators in Table 1 are given by curves in Figure 16.

Table 1. PSNRs and COUNTs under different internal noise intensities.

D	IMAGE(A)		IMAGE(B)		IMAGE(C)	
	PSNR	COUNT	PSNR	COUNT	PSNR	COUNT
0	11.3456	317	11.5689	315	11.0982	290
0.5	12.8954	320	12.7745	311	12.7745	293
1	14.3342	335	14.3862	328	14.3862	300
1.5	14.4533	343	14.5322	336	14.5322	310
2	13.3341	328	13.4531	323	13.4531	306
2.5	12.4789	322	12.5678	321	12.5678	302
3	11.8422	324	11.0986	317	11.0986	298
3.5	11.5421	320	11.9605	316	11.9605	295
4	10.7864	318	10.3432	324	10.3432	289
4.5	10.8787	321	10.9807	319	10.9807	288
5	10.8766	316	10.9877	314	10.9877	278

Referring to Table 1 and Figures 16 and 17, as D increases from 0 to 5, the values of PSNR and COUNT show a positive correlation with the increase of noise intensity. When the internal noise intensity reaches around 1.5, the maximum value appears, indicating that 1.5 is the optimal internal noise. While the internal noise shows a negative correlation between 1.5 and 5, with both curves showing a downward trend, it indicates that both indicators are correlated, but the overall fluctuation is not significant. The experimental data in Table 1 is consistent with the qualitative analysis in Figures 13–15, which further indicates that the proposed method has better robustness to internal noise.

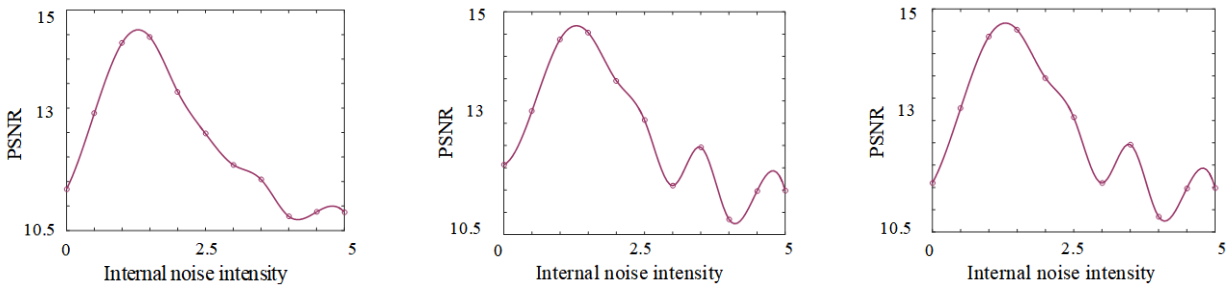

Figure 16. The values of PSNR corresponding to Table 1.

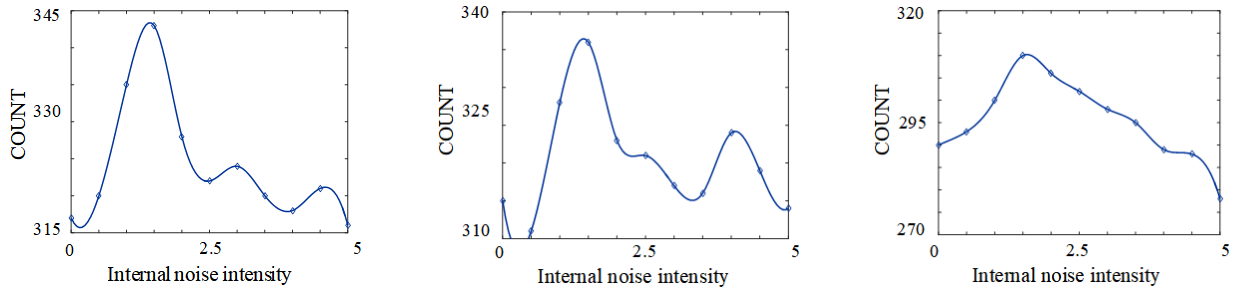

Figure 17. The values of COUNT corresponding to Table 1.

To further illustrate the advantages of the proposed method in image segmentation, Gaussian white noises with intensities of 1, 3, and 5 are added to Figure 7(a), and the five methods are used to segment the denoised images. The experimental results are shown in Figures 18–20.

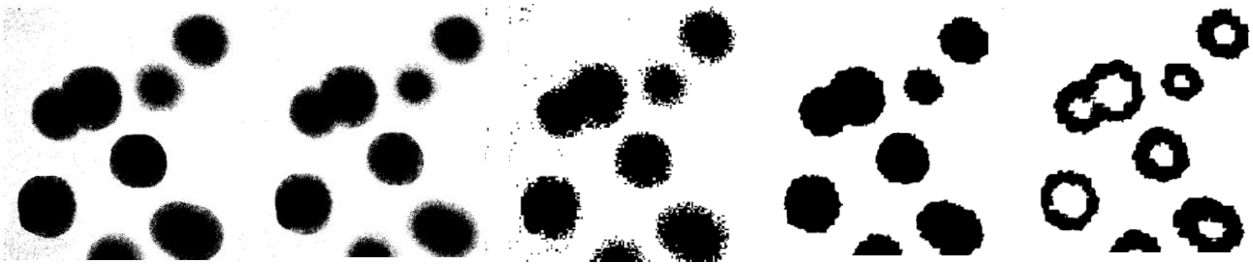

(a) ACIH. (b) HBPA. (c) UNet++. (d) Open-loop FHN network model. (e) ours.

Figure 18. Segmentation results on Figure 7(a) by different methods with external noise intensity 1.

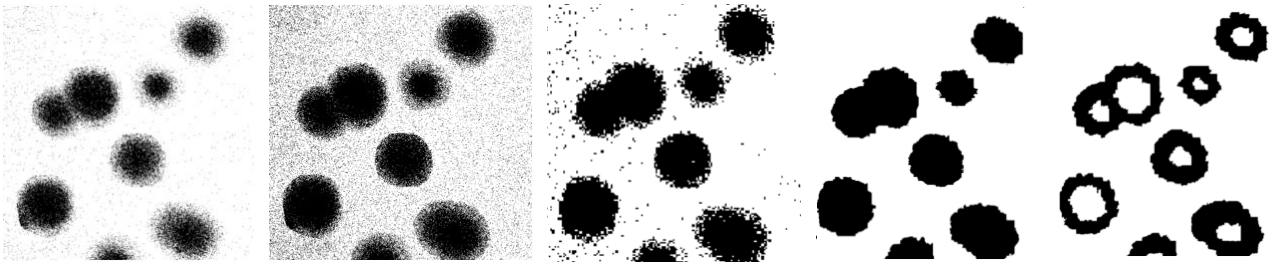

(a) ACIH. (b) HBPA. (c) UNet++. (d) Open-loop FHN network model. (e) ours.

Figure 19. Segmentation results on Figure 7(a) by different methods with external noise intensity 3.

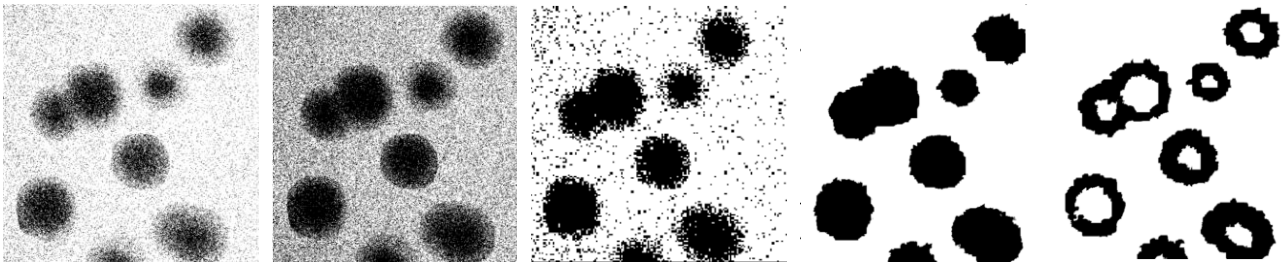

(a) ACIH. (b) HBPA. (c) UNet++. (d) Open-loop FHN network model. (e) ours.

Figure 20. Segmentation results on Figure 7(a) by different methods with external noise intensity 5.

For (a)–(c) in Figures 18–20, as the external noise intensity increases, the effectiveness of the ACIH segmentation method, HBPA method, and UNet++ method gradually deteriorates. When the external noise intensity is 5, the colony targets are basically submerged in the noise, and the

segmentation effect is not ideal. From (d), (e) in Figures 18–20, the open-loop FHN network model and the proposed method are almost unaffected by the external noise. The reason is that they both utilize the SR mechanism, which converts the noisy parts of the image into useful information of the signal, thus avoiding noise interference during segmentation. It is worth noting that although the open-loop FHN network model achieves effective segmentation of colony targets in strong noise backgrounds, it does not distinguish strong and weak contrast regions. Fortunately, the colony targets segmented by our proposed method not only maintain good geometric shape and smooth edges, but also achieve good segmentation of strong and weak contrast regions, demonstrating good robustness to external noise.

Table 2. PSNRs of different methods under different external noise intensities.

D	IMAGE(A) PSNR					IMAGE(B) PSNR					IMAGE(C) PSNR				
	ACIH	HBPA	UNet++	OPEN	OURS	ACIH	HBPA	UNet++	OPEN	OURS	ACIH	HBPA	UNet++	OPEN	OURS
0	14.6784	14.5564	14.3367	15.4452	15.4421	14.5424	14.6521	14.3877	15.6556	15.6509	14.5647	14.4521	14.3632	15.6721	15.6692
0.5	14.6542	14.6782	14.1054	15.4325	15.4316	14.5309	14.5011	14.2632	15.5532	**15.6589**	14.4041	14.4103	14.2088	15.6711	15.6653
1	14.2347	14.2566	14.0211	15.4323	**15.4325**	14.3272	14.4899	14.1033	15.4898	15.4877	14.3788	14.3256	14.0907	15.6689	**15.6992**
1.5	14.0233	14.0207	14.0132	15.4315	15.4317	14.2211	14.4376	14.0288	15.4709	**15.4845**	14.3609	14.2897	13.9325	15.6609	15.6603
2	14.0943	14.1228	13.8202	15.4232	**15.4244**	14.0907	14.4108	13.9033	15.4751	15.4721	13.9801	14.3001	13.7358	15.5078	**15.5111**
2.5	13.9602	13.7819	13.3892	15.4103	**15.4112**	13.7903	14.3581	13.4129	15.4801	15.4799	13.7678	13.7784	13.4899	15.4745	15.4728
3	13.5332	13.5623	13.3576	15.4077	**15.4148**	13.7278	13.7766	13.5072	15.4789	**15.4801**	13.7303	13.6565	13.2055	15.4667	**15.4787**
3.5	13.4755	13.3556	13.2809	15.3959	15.3901	13.4099	13.4332	13.0198	15.4745	**15.4803**	13.5109	13.2667	13.0462	15.4005	**15.4112**
4	13.3445	12.6076	13.0532	15.3906	**15.4008**	13.3789	12.4417	12.6101	15.4134	15.4099	13.4608	12.6513	12.5089	15.3908	**15.4011**
4.5	13.0123	12.3237	12.8121	15.3778	**15.3799**	13.3504	12.1531	12.1415	15.3998	**15.4013**	13.2527	12.4091	12.1566	15.3555	**15.3589**
5	12.4561	12.1611	12.1321	15.3743	**15.3802**	12.3313	12.0087	12.0109	15.3966	**15.4002**	12.9989	12.2365	12.2078	15.3891	**15.3922**

Likewise, taking PSNR as a quantitative indicator, the values of PSNR for (a), (b), and (c) in Figure 7 are calculated as external noise intensities ranging from 0 to 5, as shown in Table 2. With the increase of external noise, the PSNRs of the ACIH and HBPA methods for the three colony plots all decrease with the enhancement of external noise. Both OPEN (i.e., the open-loop FHN network model) and OURS (i.e., our proposed method) also decrease with the enhancement of external noise intensity, but the decrease is not as significant compared to the ACIH and HBPA methods. This also indicates that the open-loop and closed-loop neural network of FHN has good robustness. The PSNRs of the OPEN and OURS methods are not significantly different, but it can be seen that with the increase of noise intensity, the PSNRs of OURS are generally higher than that of the OPEN method. This is consistent with the subjective qualitative analysis results in Figures 18–20, further demonstrating that the proposed method has good robustness to external noise.

To further demonstrate the generalization capability of the proposed method, five similar colony images are processed. As seen from Figure 21, this is consistent with the experimental results mentioned above. The experimental comparison methods used exhibit good segmentation performance and are all cutting-edge algorithms at present. However, for this type of multi-layered bacterial colony images, the method proposed in this paper demonstrates relatively good segmentation performance, compensating for a scenario processing mode lacking in the compared methods. By generalizing across the five categories used, it further demonstrates the generalization ability of the proposed method. This also provides a good idea for subsequent research related to multi-feature extraction of images.

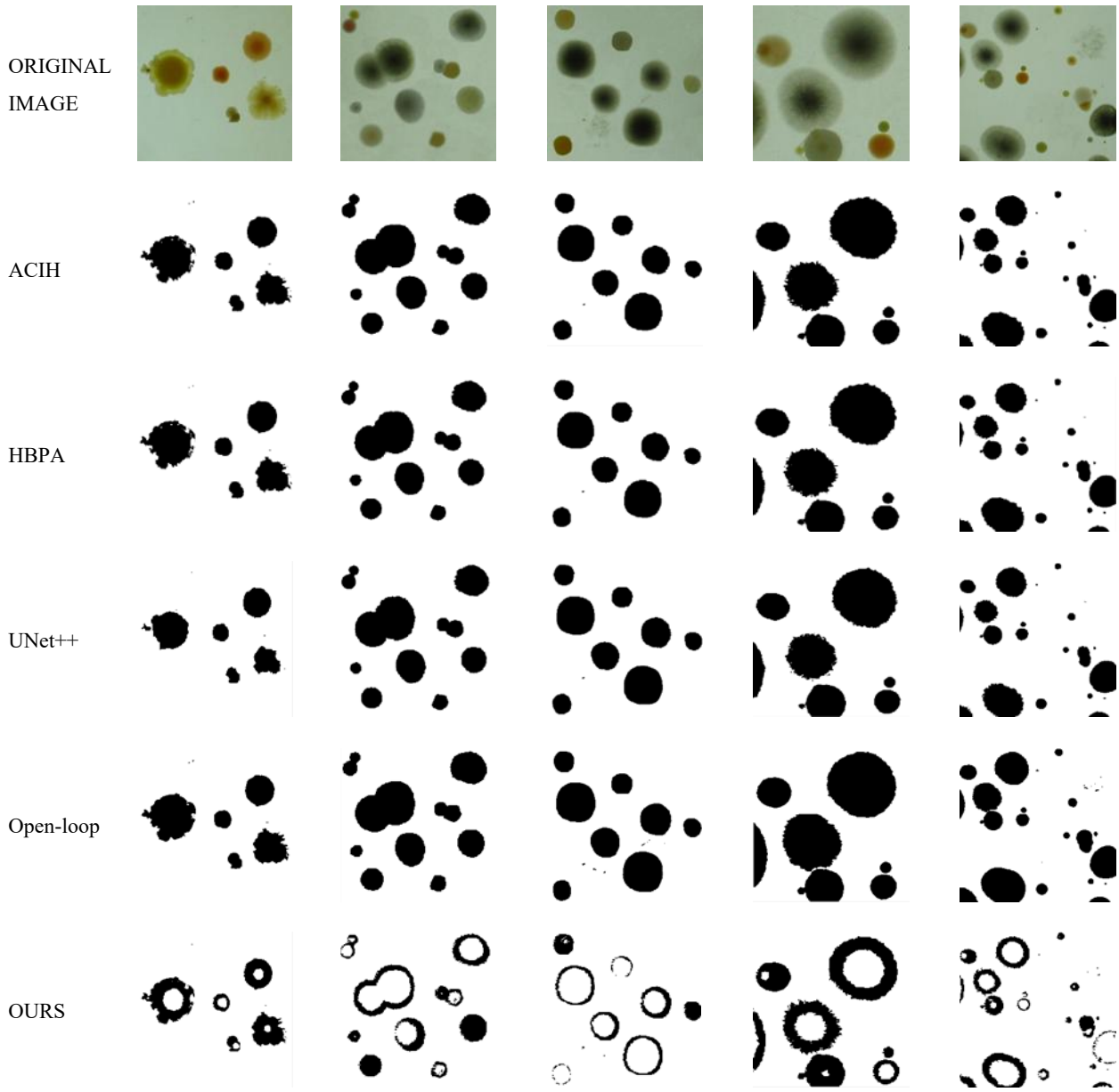

Figure 21. The results of processing five similar military colony images using different methods.

5. Ablation experiment

In order to systematically evaluate the effectiveness and necessity of each module in the proposed method, the ablation experiment analysis is conducted in this section. The experiment adopted the colony images shown in Figure 7(a) as the test objects. By gradually removing or replacing the key modules in the method, the influence of each component on the final segmentation performance is quantitatively analyzed.

The experiments first evaluate the segmentation performance under different module combinations. We label the complete method as Configuration A, and then design four ablation configurations: Configuration B removes the closed-loop design, adopting an open-loop FHN network. Configuration C removes the COA parameter optimization, using fixed SR parameters (a = 1, b = 1,

D = 1.5); Configuration D removes the Hilbert directional dimensionality reduction, using only horizontal directional scanning. Configuration E removes the SR mechanism, adopting the traditional Canny edge detector. To evaluate the segmentation quality more comprehensively, in addition to the PSNR and COUNT metrics, we introduce three standard segmentation evaluation metrics: BFScore for assessing edge detection accuracy, Dice coefficient for measuring the overlap between segmented regions and ground truth annotations, and IoU for evaluating the degree of overlap in segmented regions. Since obtaining ground truth annotations for colony images is difficult, this paper invited three experienced biologists to independently perform manual annotations on the test images in Figure 7(a), with the majority voting result used as the final ground truth reference.

The comparison of segmentation performance under each configuration is shown in Table 3. From the experimental results, it can be seen that the complete method (Configuration A) performs best across all evaluation metrics. Specifically, the removal of the closed-loop design (Configuration B) leads to a decrease of 0.151 in BFScore and 0.158 in the Dice coefficient, indicating that the closed-loop structure is crucial for simultaneously detecting edges with strong and weak contrast. The removal of COA optimization (Configuration C) reduces the BFScore by 0.058, demonstrating that adaptive parameter optimization can effectively enhance the performance of the SR system. The removal of Hilbert directional dimensionality reduction (Configuration D) results in a significant performance drop, showing that multi-directional feature extraction can more comprehensively capture image edge information. In the complete IoU scenario, the indicator clearly demonstrates a significant improvement in the accuracy of detecting hierarchical edges. When the SR mechanism is completely removed (Configuration E), the performance decline is most pronounced, with the BFScore decreasing by 0.209, which verifies the unique advantage of the SR mechanism in enhancing useful signals in noisy environments.

Table 3. Comparison of segmentation performance under different module configurations.

Configuration	BFScore	Dice	IoU	PSNR	COUNT	Time(s)
A	0.863	0.892	0.895	14.5345	343	5.34
B	0.712	0.734	0.581	13.4403	281	3.87
C	0.805	0.831	0.713	13.9816	305	2.92
D	0.743	0.769	0.625	13.6723	290	1.23
E	0.654	0.682	0.518	12.3105	215	0.45

In terms of convergence analysis, the COA algorithm recorded the changes in fitness value (i.e., the number of detected transient pulses) during the optimization process. As shown in Figure 22, the algorithm essentially converges after approximately 126 generations, demonstrating good stability. In the initial stage, the fitness value rises rapidly, then enters a plateau period, and finally stabilizes. This convergence characteristic indicates that the COA algorithm can effectively explore the parameter space and identify the parameter combination that optimizes the performance of the SR system.

As a matter of fact, the post-processing of pulse detection is crucial for reducing the false detection rate. In practical applications, noise interference may generate pseudo-peaks, affecting the accuracy of edge detection. We adopted multiple post-processing strategies: setting a minimum pulse width of 3 sampling points to eliminate excessively short noise pulses, setting a minimum peak distance of 10 sampling points to prevent false detection of adjacent peaks, and screening based on the significance of local maxima to retain prominent peaks. SR itself incorporates a de-jittering mechanism

that merges consecutive pulses occurring within a short time interval. Experiments show that after complete post-processing, the false detection rate of pulse detection decreased from 21.3% to 3.8%, while maintaining the correct detection rate of 96.8%. This post-processing strategy significantly improves the reliability of edge detection, particularly in high-noise environments.

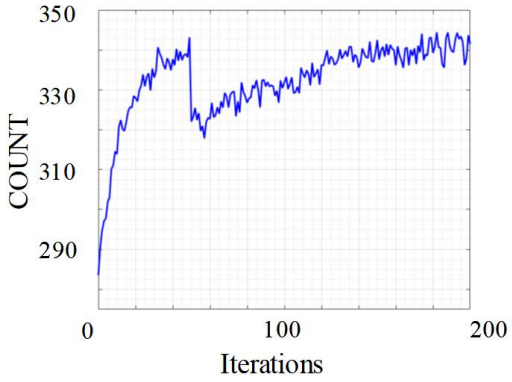

Figure 22. Convergence curve of COA algorithm (internal noise intensity D = 1.5).

The computational complexity of the method primarily stems from three components: Hilbert directional dimension reduction, closed-loop FHN network processing, and COA optimization. For an image of size M × N, the computational complexity of the Hilbert transform in four directions is O (4 × M × N); the computational complexity of closed-loop FHN network processing (involving two SR modulations) is O (2 × K × M × N), where K is the number of neurons; the computational complexity of COA optimization is O (P × T × M × N), where P is the population size and T is the number of iterations. In actual testing, the average processing time for a 512 × 512 image was 2.34 seconds (on an Intel Core i7-12700H CPU platform), with COA optimization accounting for approximately 65% of the time, the Hilbert transform about 25%, and FHN network processing about 10%. Compared to other methods, UNet++ has an inference time of about 0.15 seconds but requires extensive training data and annotation efforts. Without the need for large training samples, our method achieves acceptable processing times, especially when accelerated by GPU, reducing the time to 0.78 seconds (NVIDIA RTX 4090), nearing the requirements for practical applications. The selection of different runtime environment metrics is illustrated in Figure 23.

It should be specifically noted that in our proposed method, the SR unit primarily serves as an enhanced denoising module rather than a learning neuron. This design choice is based on the practical requirements of the application scenario. For colony image segmentation, the main challenges lie in noise suppression and edge enhancement, rather than learning complex patterns. The SR mechanism effectively enhances edge information under strong noise backgrounds by converting noise energy into useful signal energy. Although this might sacrifice some characteristics of the SR unit as a learning neuron (such as the typical bell-shaped response curve), in the current application scenario, denoising and enhancement capabilities are more critical. Our experimental results also validate the effectiveness of this design: under external noise intensity of 5, our method maintained good segmentation performance, while the performance of traditional methods declined significantly.

Based on the results of the ablation study, the following conclusions can be drawn: each module in the full method plays a vital role, and the removal of any module leads to performance degradation.

The closed-loop design enables simultaneous detection of edges with strong and weak contrast. The COA algorithm achieves adaptive optimization of SR parameters. Hilbert directional dimension reduction ensures the completeness of multi-directional features. The SR mechanism demonstrates significant advantages in noisy environments. These modules cooperate synergistically, collectively enhancing the performance of colony image segmentation. The experiments also indicate that while COA optimization increases computational cost, its contribution to performance improvement is significant. Overall, the ablation experiments verify the rationality of the proposed method's design and the effectiveness of each module.

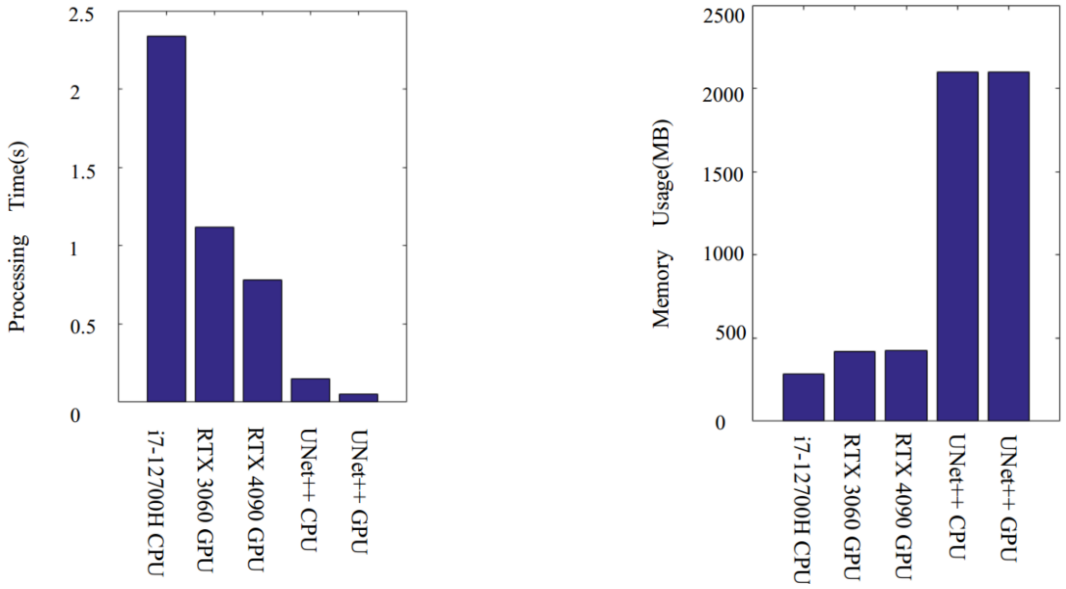

(a) Processing time comparison on different platforms. (b) Memory usage comparison on different platforms.

Figure 23. Performance indicators under different operating environments.

6. Conclusions

In this paper, we first address the strong and weak jump detection problem of one-dimensional signals by the proposed closed-loop FHN neural network model based on SR mechanism. The results show that the proposed method can adjust its internal noise to make the input signal, the internal and external noises, and the neural network interact with each other, generate SR, which enhances useful signals by using the energy of noise, for achieving synchronous detection of strong and weak jump signals under strong noise background. As for two-dimensional images, taking the colony images as an example, raster scanning and Hilbert scanning are performed to reduce the dimensionality into one-dimensional signals for further processing. Compared with the traditional methods for image segmentation, the proposed method can detect both strong and weak contrast edges. Besides, the detected edges are smoother, higher in contrast, highlight edge details, have a strong sense of hierarchy, and are more robust to the external noise. As a result, the proposed method performs well in terms of multiple contrast edges of image segmentation under strong noise background. In the future, the proposed method will be improved for edge detection of multi contrast images.

Use of AI tools declaration

The authors declare they have not used Artificial Intelligence (AI) tools in the creation of this article.

Acknowledgments

This work was supported in part by the High-level Talent Research Initiation Fund Project of Taizhou University under Grant TZXYQD2024A007 and the National Natural Science Foundation of China under Grant 12202427.

Conflict of interest

The authors declare there is no conflict of interest.

References

1. N. Yudistira, M. S. Kavitha, J. Rajan, T. Kurita, Attention-effective multiple instance learning on weakly stem cell colony segmentation, *Intell. Syst. Appl.*, **17** (2023), 200187. https://doi.org/10.1016/j.iswa.2023.200187
2. C. Spahn, E. Gómez-de-Mariscal, R. F. Laine, P. M. Pereira, L. von Chamier, M. Conduit, et al., DeepBacs for multi-task bacterial image analysis using open-source deep learning approaches, *Commun. Biol.*, **5** (2022), 688. https://doi.org/10.1038/s42003-022-03634-z
3. P. Ma, C. Li, M. M. Rahaman, Y. Yao, J. Zhang, S. Zou, et al., A state-of-the-art survey of object detection techniques in microorganism image analysis: from classical methods to deep learning approaches, *Artif. Intell. Rev.*, **56** (2023), 1627–1698. https://doi.org/10.1007/s10462-022-10209-1
4. A. Soni, A. Rai, CT scan based brain tumor recognition and extraction using Prewitt and morphological dilation, in *2021 International Conference on Computer Communication and Informatics (ICCCI)*, (2021), 1–6. https://doi.org/10.1109/ICCCI50826.2021.9402677
5. R. V. Patil, R. Aggarwal, G. M. Poddar, M. Bhowmik, M. K. Patil, Embedded integration strategy to image segmentation using canny edge and K-means algorithm, *SSRN Electron. J.*, **12** (2024), 1–8. https://doi.org/10.2139/ssrn.5095501
6. Y. Su, W. Tan, Y. Dong, W. Xu, P. Huang, J. Zhang, et al., Enhancing concealed object detection in Active Millimeter Wave Images using wavelet transform, *Signal Process.*, **216** (2024), 109303. https://doi.org/10.1016/j.sigpro.2023.109303
7. S. Ghosh, S. Das, Multi-scale morphology-aided deep medical image segmentation, *Eng. Appl. Artif. Intell.*, **137** (2024), 109047. https://doi.org/10.1016/j.engappai.2024.109047
8. H. Cui, X. Zheng, W. Zeng, R. Ma, Y. Zhang, Q. Yin, et al., Intuitionistic fuzzy local information C-means algorithm for image segmentation, *Inf. Sci.*, **681** (2024), 121205. https://doi.org/10.1016/j.ins.2024.121205
9. H. Ziang, J. Zhang, L. Li, Framework for lung CT image segmentation based on UNet++, preprint, arXiv:2501.02428.
10. S. Rezvani, M. Fateh, Y. Jalali, A. Fateh, FusionLungNet: Multi-scale fusion convolution with refinement network for lung CT image segmentation, *Biomed. Signal Process. Control*, **107** (2025), 107858. https://doi.org/10.1016/j.bspc.2025.107858

11. Z. Zhu, M. Sun, G. Qi, Y. Li, X. Gao, Y. Liu, Sparse dynamic volume TransUNet with multi-level edge fusion for brain tumor segmentation, *Comput. Biol. Med.*, **172** (2024), 108284. https://doi.org/10.1016/j.compbiomed.2024.108284
12. T. Chen, Cell image segmentation method based on convolution neural network, in *2019 IEEE 5th International Conference on Computer and Communications (ICCC)*, (2019), 1765–1770. https://doi.org/10.1109/ICCC47050.2019.9064436
13. J. Du, Y. Zhang, X. Jin, X. Zhang, A cell image segmentation method based on edge feature residual fusion, *Methods*, **219** (2023), 111–118. https://doi.org/10.1016/j.ymeth.2023.09.009
14. M. E. Cek, I. F. Uludag, Spectral resonance in Fitzhugh-Nagumo neuron system: relation with stochastic resonance and its role in EMG signal characterization, *Cogn. Neurodyn.*, **18** (2024), 1779–1787. https://doi.org/10.1007/s11571-023-10043-3
15. M. Ge, K. Jia, X. Wang, Y. Liu, Y. Jiang, Researches on dynamics and noise effects of FHN neuron based on memristor-memcapacitor coupling, *Nonlinear Dyn.*, **113** (2025), 26671–26693. https://doi.org/10.1007/s11071-025-11454-z
16. K. Wu, J. Li, Effects of high-low-frequency electromagnetic radiation on vibrational resonance in FitzHugh-Nagumo neuronal systems, *Eur. Phys. J. B*, **96** (2023), 126. https://doi.org/10.1140/epjb/s10051-023-00594-z
17. C. Laing, G. J. Lord, *Stochastic Methods in Neuroscience*, Oxford University Press, 2009. https://doi.org/10.1093/acprof:oso/9780199235070.001.0001
18. H. Zhang, J. Yu, Y. Ma, Z. Pan, J. Zhao, Image restoration based on stochastic resonance in a parallel array of Fitzhugh-Nagumo neuron, *Complexity*, **2020** (2020), 8843950. https://doi.org/10.1155/2020/8843950
19. M. Dehghani, Z. Montazeri, E. Trojovská, P. Trojovský, Coati optimization algorithm: A new bio-inspired metaheuristic algorithm for solving optimization problems, *Knowl.-based Syst.*, **259** (2023), 110011. https://doi.org/10.1016/j.knosys.2022.110011
20. P. Kandhway, A novel adaptive contextual information-based 2D-histogram for image thresholding, *Expert Syst. Appl.*, **238** (2024), 122026. https://doi.org/10.1016/j.eswa.2023.122026
21. K. Manikandan, B. Sudhakar, Optimized multi-threshold image segmentation using a hybrid bee-pollinator algorithm, *Syst. Soft Comput.*, **7** (2025), 200404. https://doi.org/10.1016/j.sasc.2025.200404
22. D. R. I. M. Setiadi, PSNR vs SSIM: imperceptibility quality assessment for image steganography, *Multimed. Tools Appl.*, **80** (2021), 8423–8444. https://doi.org/10.1007/s11042-020-10035-z
23. Y. Al Najjar, Comparative analysis of image quality assessment metrics: MSE, PSNR, SSIM and FSIM, *Int. J. Sci. Res.*, **13** (2024), 110–114. https://doi.org/10.21275/SR24302013533

AIMS Press